INTERNATIONAL JOURNAL OF
ENERGY AND ENVIRONMENT

Volume 3, Issue 2, 2012 pp.161-180

Journal homepage: www.IJEE.IEEFoundation.org

Novel design of a disk-shaped compacted micro-structured air-breathing PEM fuel cell

Maher A.R. Sadiq Al-Baghdadi

Fuel Cell Research Center, International Energy & Environment Foundation, Al-Najaf, P.O.Box 39, Iraq.

Abstract

The presence of microelectromechanical system (MEMS) technology makes it possible to manufacture the miniaturized fuel cell systems for application in portable electronic devices. The majority of research on micro-scale fuel cells is aimed at micro-power applications. There are many new miniaturized applications which can only be realized if a higher energy density power source is available compared to button cells and other small batteries. In small-scale applications, the fuel cell should be exceptionally small and have highest energy density. One way to achieve these requirements is to reduce the thickness of the cell (compacted-design) for increasing the volumetric power density of a fuel cell power supply.

A novel, simple to construct, air-breathing micro-structured PEM fuel cell which work in still or slowly moving air has been developed. The novel geometry enables optimum air access to the cathode without the need for pumps, fans or similar devices. In addition, the new design can achieve much higher active area to volume ratios, and hence higher volumetric power densities. Three-dimensional, multi-phase, non-isothermal CFD model of this novel design has been developed. This comprehensive model account for the major transport phenomena in an air-breathing micro-structured PEM fuel cell: convective and diffusive heat and mass transfer, electrode kinetics, transport and phase-change mechanism of water, and potential fields. The model is shown to understand the many interacting, complex electrochemical, and transport phenomena that cannot be studied experimentally. Fully three-dimensional results of the species profiles, temperature distribution, potential distribution, and local current density distribution are presented and analyzed with a focus on the physical insight and fundamental understanding. They can provide a solid basis for optimizing the geometry of the PEM micro fuel cell stack running with a passive mode.

Copyright © 2012 International Energy and Environment Foundation - All rights reserved.

Keywords: Ambient air-breathing, Fuel cell modelling, CFD, Compacted-design Micro-PEM fuel cell, Disk-shaped.

1. Introduction

Fuel cells are growing in importance as sources of sustainable energy and will doubtless form part of the changing programme of energy resources in the future. Small fuel cells have provided significant advantages in portable electronic applications over conventional battery systems. However, the typical polymer electrolyte fuel cell system with its heavy reliance on subsystems for cooling, humidification and air supply would not be practical in small applications. The air-breathing proton exchange membrane (PEM) fuel cells without moving parts (external humidification instrument, fans or pumps) are one of the most competitive candidates for future portable-power applications. A key advantage of fuel cells for

such applications is the much longer continuous operation and almost instantaneous refuelling (as opposed to the recharging time required by batteries). The viability of PEM fuel cells as battery replacements requires that PEM fuel cells undergo significant miniaturization while achieving higher power densities. This presents challenges for small scale and micro-fuel cells in terms of design, materials, effective transport of reactants, and heat management.

The development of physically representative models that allow reliable simulation of the processes under realistic conditions is essential to the development and optimization of fuel cells, the introduction of cheaper materials and fabrication techniques, and the design and development of novel architectures which enhance volumetric power density. The difficult experimental environment of fuel cell systems has stimulated efforts to develop models that could simulate and predict multi-dimensional coupled transport of reactants, heat and charged species using computational fluid dynamic (CFD) methods.

Several studies have been reported on the performance and design of air-breathing PEM fuel cells. Litster and Djilali [1] developed a single-phase one-dimensional semi-analytical model of the membrane electrode assembly (MEA) of planar air-breathing PEM fuel cells for portable devices. Their study suggests that improved performance of air-breathing fuel cells can be achieved by increasing the heat removal rate and thus promoting higher relative humidity levels in the gas diffusion layer (GDL). O'Hayre et al. [2] developed a one-dimensional, non-isothermal model that capture the coupling between water generation, oxygen consumption, self-heating and natural convection at the cathode of an air breathing fuel cell. Their result confirms the strong effect of self-heating on the water balance within passive air-breathing fuel cells. Rajani and Kolar [3] developed a single-phase two-dimensional model for a planar air-breathing PEM fuel cell that considered both heat and mass transfer. Their results showed that the maximum power density and the corresponding current density increase with decreasing height of the fuel cell, decreasing ambient temperature and increasing ambient relative humidity. Hwang et al. [4] developed a single-phase 3D model of coupled fluid flow field, mass transport and electrochemistry in an air-breathing cathode of a planar PEM fuel cell. In their results, electrochemical/mass characteristics such as flow velocities, species mass fraction, species flux and current density distributions in a passive cathode have been discussed in detail. Al-Baghdadi [5] developed a multiphase three-dimensional CFD model for a planar air-breathing PEM fuel cell that considered both heat and mass transfer in addition to the phase-change. The study showed that the oxygen transport limitation plays a great role in the performance of air-breathing fuel cells.

However, these fuel cell designs have generally relied on traditional planar MEA architecture. Because the majority of PEM fuel cell designs are based on planar plate and frame architecture, their volumetric power densities are inherently constrained by their two-dimensional active area.

This work introduces a novel disk-shaped micro-structured air-breathing PEM fuel cell. The new design can achieve much higher active area to volume ratios, and hence higher volumetric power densities. In this design, the MEA played an additional function by forming the channels that distribute the fuel and oxidant. Thus, the volume that previously comprised the flow channels could support additional active area and generate increased volumetric power density. The height of the gas diffusion layers (GDLs) decreases along the main flow direction and this leads to improve the gases flow and diffusion through the porous layers, and hence improve the cell performance. Such fuel cells have the potential to be significantly cheaper, smaller, and lighter than tubular and planar plate and frame fuel cells; they could also broaden the range of fuel cell applications.

2. Model description

The present work presents a comprehensive three–dimensional, multi–phase, non-isothermal model of a new design air-breathing micro-structured PEM fuel cell that incorporates the significant physical processes and the key parameters affecting fuel cell performance. The model accounts for both gas and liquid phase in the same computational domain, and thus allows for the implementation of phase change inside the gas diffusion layers. The model includes the transport of gaseous species, liquid water, protons, and energy. Water transport inside the porous gas diffusion layer and catalyst layer is described by two physical mechanisms: viscous drag and capillary pressure forces, and is described by advection within the gas channels. Water transport across the membrane is also described by two physical mechanisms: electro-osmotic drag and diffusion.

 ©2012 International Energy & Environment Foundation. All rights reserved.

2.1 Computational domain

The full computational domain consists of a back-plate hydrogen feed chamber, and the membrane electrode assembly is shown in Figure 1. The cathode of the cell is directly open to ambient air. The oxygen needed by the fuel cell reaction is transferred by natural convection and diffusion through the gas diffusion backing into the cathode electrode.

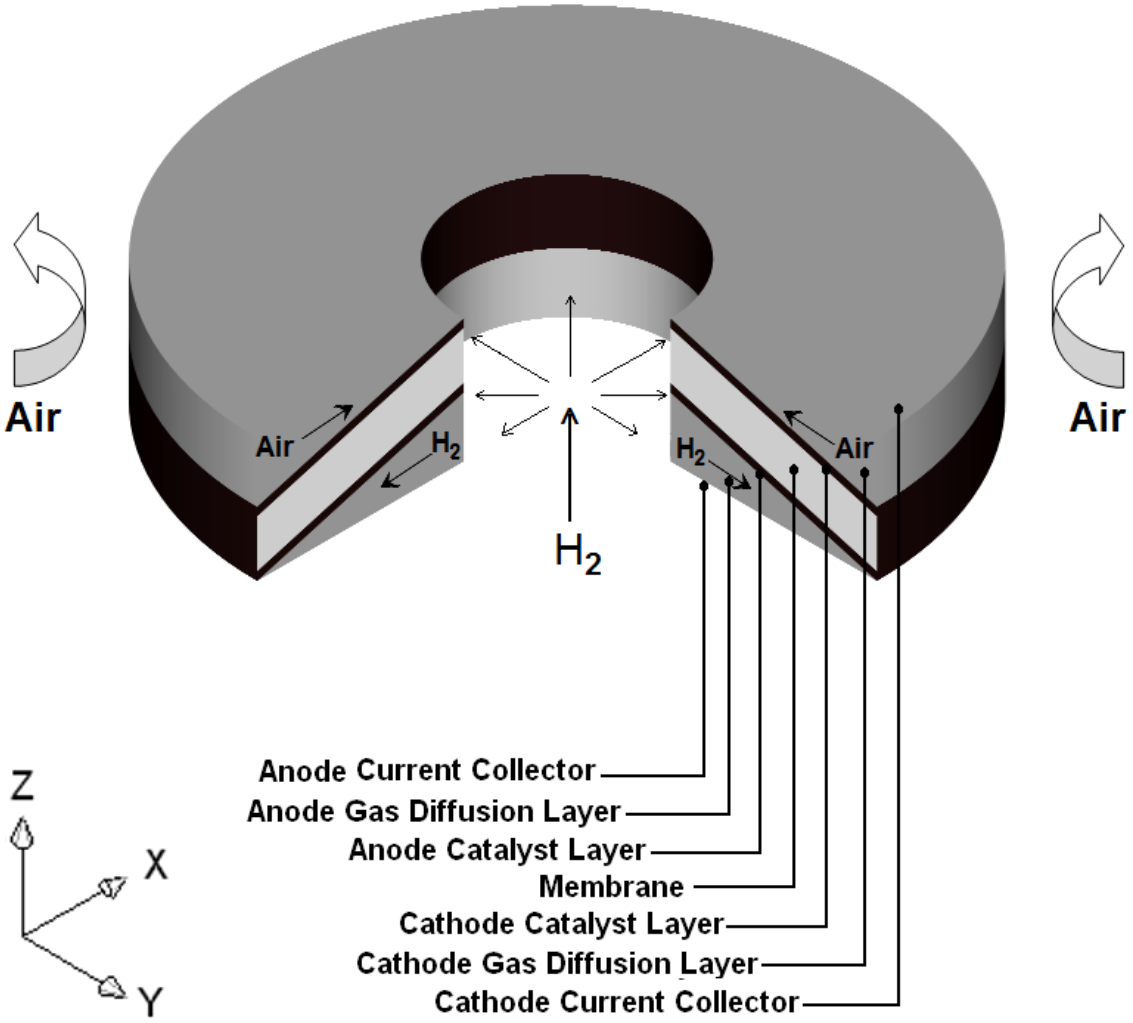

Figure 1. Three-dimensional computational domain of the disk-shaped micro-structured air-breathing PEM fuel cell

2.2 Model equations

2.2.1 Air and fuel gas flow

In natural convection region, the transport equations solved in the ambient air include continuity, momentum, energy and mass transport equations. In the fuel channel, the gas-flow field is obtained by solving the steady-state Navier-Stokes equations, i.e. the continuity equation, the mass conservation equation for each phase yields the volume fraction (r) and along with the momentum equations the pressure distribution inside the channel. The continuity equation for the gas phase inside the channel is given by;

$$\nabla \cdot \left(r_g \rho_g \mathbf{u}_g \right) = 0 \tag{1}$$

and for the liquid phase inside the channel becomes;

 ©2012 International Energy & Environment Foundation. All rights reserved.

$$\nabla \cdot \left(r_l \rho_l \mathbf{u}_l \right) = 0 \tag{2}$$

where $\boldsymbol{u}$ is velocity vector (m/s), ρ is density (kg/m^3). Subscript (g) is a gas phase and (l) is a liquid phase.

Two sets of momentum equations are solved in the channel, and they share the same pressure field. Under these conditions, it can be shown that the momentum equations becomes;

$$\nabla \cdot \left(\rho_g \mathbf{u}_g \otimes \mathbf{u}_g - \mu_g \nabla \mathbf{u}_g \right) = -\nabla r_g \left(P + \frac{2}{3} \mu_g \nabla \cdot \mathbf{u}_g \right) + \nabla \cdot \left[\mu_g \left(\nabla \mathbf{u}_g \right)^T \right] \tag{3}$$

$$\nabla \cdot \left(\rho_l \mathbf{u}_l \otimes \mathbf{u}_l - \mu_l \nabla \mathbf{u}_l \right) = -\nabla r_l \left(P + \frac{2}{3} \mu_l \nabla \cdot \mathbf{u}_l \right) + \nabla \cdot \left[\mu_l \left(\nabla \mathbf{u}_l \right)^T \right] \tag{4}$$

where P is pressure (Pa), μ is viscosity [kg/(m·s)].
The mass balance is described by the divergence of the mass flux through diffusion and convection. Multiple species are considered in the gas phase only, and the species conservation equation in multi-component, multi-phase flow can be written in the following expression for species i;

$$\nabla \cdot \left[- r_g \rho_g y_i \sum_{j=1}^{N} D_{ij} \frac{M}{M_j} \left[\left(\nabla y_j + y_j \frac{\nabla M}{M} \right) + \left(x_j - y_j \right) \frac{\nabla P}{P} \right] + r_g \rho_g y_i \cdot \mathbf{u}_g + D_i^T \frac{\nabla T}{T} \right] = 0 \tag{5}$$

where T is temperature (K), y is mass fraction, x is mole fraction. Subscript i denotes oxygen at the cathode side and hydrogen at the anode side, and j is water vapour in both cases. Nitrogen is the third species at the cathode side.

The Maxwell-Stefan diffusion coefficients of any two species are dependent on temperature and pressure. They can be calculated according to the empirical relation based on kinetic gas theory [6];

$$D_{ij} = \frac{T^{1.75} \times 10^{-3}}{P \left[\left(\sum_k V_{ki} \right)^{1/3} + \left(\sum_k V_{kj} \right)^{1/3} \right]^2} \left[\frac{1}{M_i} + \frac{1}{M_j} \right]^{1/2} \tag{6}$$

In this equation, pressure is in [atm] and the binary diffusion coefficient is in [cm^2/s]. The values for $\left(\sum V_{ki} \right)$ are given by Fuller et al. [6].
The temperature field is obtained by solving the convective energy equation;

$$\nabla \cdot \left(r_g \left(\rho_g C p_g \mathbf{u}_g T - k_g \nabla T \right) \right) = 0 \tag{7}$$

where Cp_g is a specific heat capacity (J/(kg.K)), and k_g is gases thermal conductivity (W/(m.K)).

The gas phase and the liquid phase are assumed to be in thermodynamic equilibrium; hence the temperature of the liquid water is the same as the gas phase temperature.

2.2.2 Gas diffusion layers

The physics of multiple phases through a porous medium is further complicated here with phase change and the sources and sinks associated with the electrochemical reaction. The equations used to describe transport in the gas diffusion layers are given below. Mass transfer in the form of evaporation ($\dot{m}_{phase} > 0$) and condensation ($\dot{m}_{phase} < 0$) is assumed. Where $\dot{m}_{phase}$ is mass transfer: for evaporation ($\dot{m}_{phase} = \dot{m}_{evap}$) and for condensation ($\dot{m}_{phase} = \dot{m}_{cond}$) (kg/s).
So that the mass balance equations for both phases are;

$$\nabla \cdot \left((1 - sat) \rho_g \varepsilon \mathbf{u}_g \right) = \dot{m}_{phase} \tag{8}$$

 ©2012 International Energy & Environment Foundation. All rights reserved.

$$\nabla \cdot \left(sat.\rho_l \varepsilon \mathbf{u}_l \right) = \dot{m}_{phase} \tag{9}$$

where *sat* is saturation, ε is porosity.

The momentum equation for the gas phase reduces to Darcy's law, which is, however, based on the relative permeability for the gas phase (KP). The relative permeability accounts for the reduction in pore space available for one phase due to the existence of the second phase [7].
The momentum equation for the gas phase inside the gas diffusion layer becomes;

$$\mathbf{u}_g = -(1-sat)\frac{Kp}{\mu_g}\nabla P \tag{10}$$

where *Kp* is hydraulic permeability (m^2).

Two liquid water transport mechanisms are considered; shear, which drags the liquid phase along with the gas phase in the direction of the pressure gradient, and capillary forces, which drive liquid water from high to low saturation regions [7]. Therefore, the momentum equation for the liquid phase inside the gas diffusion layer becomes;

$$\mathbf{u}_l = -\frac{KP_l}{\mu_l}\nabla P + \frac{KP_l}{\mu_l}\frac{\partial P_c}{\partial sat}\nabla sat \tag{11}$$

where P_c is capillary pressure (Pa).

The functional variation of capillary pressure with saturation is calculated as follows [7];

$$P_c = \sigma\left(\frac{\varepsilon}{KP}\right)^{1/2}\left(1.417(1-sat) - 2.12(1-sat)^2 + 1.263(1-sat)^3\right) \tag{12}$$

where σ is surface tension (N/m).

The liquid phase consists of pure water, while the gas phase has multi components. The transport of each species in the gas phase is governed by a general convection-diffusion equation in conjunction which the Stefan-Maxwell equations to account for multi species diffusion;

$$\nabla \cdot \left[\begin{array}{r} -(1-sat)\rho_g \varepsilon y_i \sum_{j=1}^{N} D_{ij}\frac{M}{M_j}\left[\left(\nabla y_j + y_j\frac{\nabla M}{M}\right) + \left(x_j - y_j\right)\frac{\nabla P}{P}\right] + \\ (1-sat)\rho_g \varepsilon y_i \cdot \mathbf{u}_g + \varepsilon D_i^T \frac{\nabla T}{T} \end{array} \right] = \dot{m}_{phase} \tag{13}$$

In order to account for geometric constraints of the porous media, the diffusivities are corrected using the Bruggemann correction formula [8, 9];

$$D_{ij}^{eff} = D_{ij} \times \varepsilon^{1.5} \tag{14}$$

The heat transfer in the gas diffusion layers is governed by the energy equation as follows;

$$\nabla \cdot \left((1-sat)\left(\rho_g \varepsilon Cp_g \mathbf{u}_g T - k_{eff,g}\varepsilon \nabla T\right)\right) = \varepsilon\beta\left(T_{solid} - T\right) - \varepsilon \dot{m}_{phase}\Delta H_{evap} \tag{15}$$

where k_{eff} is effective electrode thermal conductivity (W/m·K), the term ($\varepsilon\beta\left(T_{solid} - T\right)$), on the right hand side, accounts for the heat exchange to and from the solid matrix of the GDL. β is a modified heat transfer coefficient that accounts for the convective heat transfer in [W/m^2] and the specific surface area [m^2/m^3] of the porous medium [10]. Hence, the unit of β is [W/m^3]. The gas phase and the liquid phase are assumed to be in thermodynamic equilibrium, i.e., the liquid water and the gas phase are at the same temperature.

 ©2012 International Energy & Environment Foundation. All rights reserved.

The potential distribution in the gas diffusion layers is governed by;

$$\nabla \cdot (\lambda_e \nabla \phi) = 0 \tag{16}$$

where λ_e is electrode electronic conductivity (S/m).

In order to account for the magnitude of phase change inside the GDL, expressions are required to relate the level of over- and undersaturation as well as the amount of liquid water present to the amount of water undergoing phase change. In the present work, the procedure of the current author in his previous paper [10] was used to account for the magnitude of phase change inside the GDL.

2.2.3 Catalyst layers

The catalyst layer is treated as a thin interface, where sink and source terms for the reactants are implemented. Due to the infinitesimal thickness, the source terms are actually implemented in the last grid cell of the porous medium. At the cathode side, the sink term for oxygen is given by;

$$S_{O_2} = -\frac{M_{O_2}}{4F} i_c \tag{17}$$

where M is molecular weight (kg/mole), F is Faraday's constant = 96487 (C/mole), i is local current density (A/m^2).

Whereas the sink term for hydrogen is specified as;

$$S_{H_2} = -\frac{M_{H_2}}{2F} i_a \tag{18}$$

The production of water is modelled as a source terms, and hence can be written as;

$$S_{H_2O} = \frac{M_{H_2O}}{2F} i_c \tag{19}$$

The generation of heat in the cell is due to entropy changes as well as irreversibilities due to the activation overpotential [11];

$$\dot{q} = \left[\frac{T(-\Delta s)}{n_e F} + \eta_{act} \right] i \tag{20}$$

where η_{act} is activation over potential (V), n_e is number of electrons transfer, ΔS is entropy change of cathode side reaction.

The local current density distribution in the catalyst layers is modelled by the Butler-Volmer equation [7-9];

$$i_c = i_{o,c}^{ref} \left(\frac{C_{O_2}}{C_{O_2}^{ref}} \right) \left[\exp\left(\frac{\alpha_a F}{RT} \eta_{act,c} \right) + \exp\left(-\frac{\alpha_c F}{RT} \eta_{act,c} \right) \right] \tag{21}$$

$$i_a = i_{o,a}^{ref} \left(\frac{C_{H_2}}{C_{H_2}^{ref}} \right)^{1/2} \left[\exp\left(\frac{\alpha_a F}{RT} \eta_{act,a} \right) + \exp\left(-\frac{\alpha_c F}{RT} \eta_{act,a} \right) \right] \tag{22}$$

where C_{H_2} is local hydrogen concentration (mole/m^3), $C_{H_2}^{ref}$ is reference hydrogen concentration (mole/m^3), C_{O_2} is local oxygen concentration (mole/m^3), $C_{O_2}^{ref}$ is reference oxygen concentration (mole/m^3), C_p is specific heat capacity [J/(kg·K)], D is diffusion coefficient (m^2/s), $i_{o,a}^{ref}$ is anode reference exchange current density, $i_{o,c}^{ref}$ is cathode reference exchange current density, R is

 ©2012 International Energy & Environment Foundation. All rights reserved.

universal gas constant (=8.314 J/(mole·K)), s is specific entropy [J/(mole·K)], α_a is charge transfer coefficient, anode side, and α_c is charge transfer coefficient, cathode side.

2.2.4 Membrane

The balance between the electro-osmotic drag of water from anode to cathode and back diffusion from cathode to anode yields the net water flux through the membrane;

$$N_W = n_d M_{H_2O} \frac{i}{F} - \nabla \cdot \left(\rho D_W \nabla c_W\right) \tag{23}$$

where N_w is net water flux across the membrane (kg/m^2·s), n_d is electro-osmotic drag coefficient.
The water diffusivity in the polymer can be calculated as follow [12];

$$D_W = 1.3 \times 10^{-10} \exp\left[2416\left(\frac{1}{303} - \frac{1}{T}\right)\right] \tag{24}$$

The variable c_W represents the number of water molecules per sulfonic acid group (i.e. $\text{mol}\, H_2O / \text{equivalent}\, SO_3^{-1}$).The water content in the electrolyte phase is related to water vapour activity via [13];

$$\begin{aligned} c_W &= 0.043 + 17.81a - 39.85a^2 + 36.0a^3 && (0 < a \le 1) \\ c_W &= 14.0 + 1.4(a-1) && (1 < a \le 3) \\ c_W &= 16.8 && (a \ge 3) \end{aligned} \tag{25}$$

The water vapour activity given by;

$$a = \frac{x_W P}{P_{sat}} \tag{26}$$

Heat transfer in the membrane is governed by;

$$\nabla \cdot \left(k_{mem} \cdot \nabla T\right) = 0 \tag{27}$$

where k_{mem} is membrane thermal conductivity [W/(m·K)].

The potential loss in the membrane is due to resistance to proton transport across membrane, and is governed by;

$$\nabla \cdot \left(\lambda_m \nabla \phi\right) = 0 \tag{28}$$

where λ_m is membrane ionic conductivity (S/m).

3. Results and discussion

Boundary conditions have to be applied for all variables of interest in computational domain. At the inlets of the gas-flow channel, the incoming velocity is calculated as a function of the desired current density and stoichiometric flow ratio. At the outlets, the pressure is prescribed for the momentum equation and a zero-gradient condition is imposed for all scalar equations. At the external surfaces of the cell, the convective heat transfer flux is applied. Combinations of Dirichlet and Neumann boundary conditions are used to solve the electronic and protonic potential equations. Dirichlet boundary conditions are applied at the the cathode and anode current collectors. Neumann boundary conditions are applied at the interface between the gas inlet surfaces and the gas diffusion layers to give zero potential flux into the gas inlet surfaces. Similarly, the protonic potential field requires a set of potential boundary condition and zero flux boundary condition at the anode catalyst layer interface and cathode catalyst layer interface respectively.
An initial guess of the activation overpotential is obtained from the desired current density using the Butler-Volmer equation. Then follows by computing the flow fields for each phase for velocities u,v,w,

 ©2012 International Energy & Environment Foundation. All rights reserved.

and pressure P. Once the flow field is obtained, the mass fraction equations are solved for the mass fractions of oxygen, hydrogen, nitrogen, and water. Scalar equations are solved last in the sequence of the transport equations for the temperature field in the cell and potential fields in the gas diffusion layers and the membrane. The local current densities are solved based on the Butler-Volmer equation. Convergence criteria are then performed on each variable and the procedure is repeated until convergence. The properties are updated after each global iterative loop based on the new local gas composition and temperature. Source terms reflect changes in the overall gas phase mass flow due to consumption or production of gas species via reaction and due to mass transfer between water in the vapour phase and water that is in the liquid phase or dissolved in the polymer (phase-change).

The governing equations were discretized using a finite volume method and solved using multi-physics CFD code. Stringent numerical tests were performed to ensure that the solutions were independent of the grid size. A computational quadratic finer mesh consisting of a total of 17298 nodes and 197387 meshes ware found to provide sufficient spatial resolution (Figure 2). The coupled set of equations was solved iteratively, and the solution was considered to be convergent when the relative error in each field between two consecutive iterations was less than 1.0×10^{-6}. The calculations presented here have all been obtained on a Pentium IV PC (3 GHz, 2GB RAM) using Windows XP operating system. The number of iterations required to obtain converged solutions dependent on the nominal current density of the cell; the higher the load the slower the convergence.

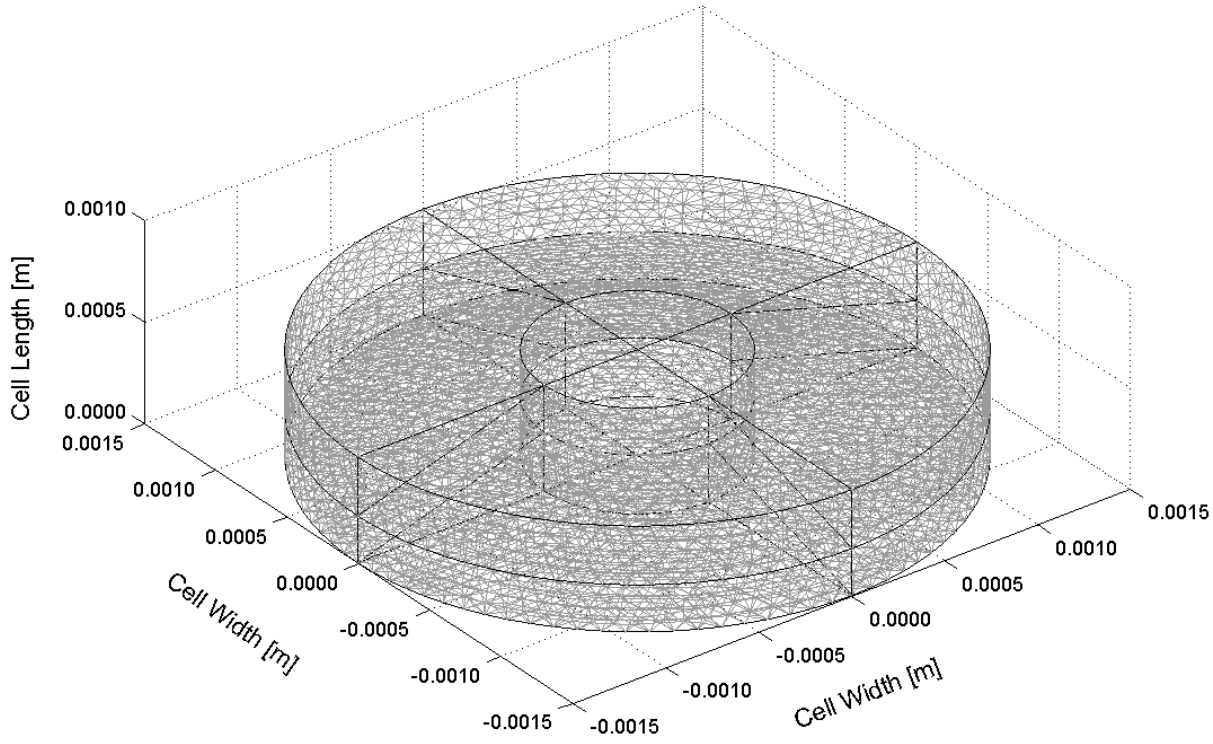

Figure 2. Computational mesh of the disk-shaped micro-structured air-breathing PEM fuel cell (quadratic)

The values of the electrochemical transport parameters for the base case operating conditions are taken from ref. [10] and are listed in Table 1. The geometric and the base case operating conditions are listed in Table 2. In order to gain some insight into the new design of the air-breathing micro-structured PEM fuel cell, the oxygen and hydrogen distribution, local current densities, temperature distribution, and potential distribution are plotted in Figures 3-10, respectively, for two different nominal current densities.

The detailed distribution of oxygen mass fraction for two different nominal current densities is shown in Figure 3. The concentration of oxygen at the catalyst layer is balanced by the oxygen that is being consumed and the amount of oxygen that diffuses towards the catalyst layer driven by the concentration gradient. The lower diffusivity of the oxygen along with the low concentration of oxygen in ambient air results in noticeable oxygen depletion near the catalyst layer. The non-linear drop in concentration along the cell width of the electrode is the result of oxygen consumption along the diffusion pathway. Although

 ©2012 International Energy & Environment Foundation. All rights reserved.

the reduction in oxygen concentration is significant, the fuel cell is still far from being starved of oxygen. The local current density of the cathode side reaction depends directly on the oxygen concentration. At a low current density, the oxygen consumption rate is low enough not to cause diffusive limitations, whereas at a high current density the concentration of oxygen at the end of the cell width of the electrode has already reached low values. It becomes clear that the diffusion of the oxygen towards the catalyst layer is the main impediment for reaching high current densities. Due to the relatively low diffusivity of the oxygen compared with that of the hydrogen, the cathode operation conditions usually determine the limiting current density. This is because an increase in current density corresponds to an increase in oxygen consumption, shown in equation (21).

The hydrogen mass fraction distribution in the anode side is shown in Figure 4 for two different nominal current densities. In general, the hydrogen concentration decreases from inlet to outlet as it is being consumed. The decrease in mass concentration of the hydrogen across the anode gas diffusion layer is smaller than for the oxygen in cathode side due to the higher diffusivity of the hydrogen.

Thermal management is required to remove the heat produced by the electrochemical reaction in order to prevent drying out of the membrane and excessive thermal stresses that may result in rupture of the membrane or mechanical damage in the cell [14-17]. The small temperature differential between the fuel cell stack and the operating environment make thermal management a challenging problem in PEM fuel cells [18-19]. The temperature distribution inside the fuel cell has important effects on nearly all transport phenomena, and knowledge of the magnitude of temperature increases due to irreversibilities might help preventing failure. Figure 5 shows the distribution of the temperature (in K) inside the cell for two different nominal current densities. The result shows that the increase in temperature can exceed several degrees Kelvin near the catalyst layer regions, where the electrochemical activity is highest. The temperature peak appears in the cathode catalyst layer, implying that major heat generation takes place in the region. In general, the temperature at the cathode side is higher than that at the anode side; this is due to the reversible and irreversible entropy production.

Table 1. Electrode and membrane parameters for base case operating conditions

Parameter	**Sym.**	**Value**	**Unit**
Electrode porosity	ε	0.4	-
Electrode electronic conductivity	λ_e	100	S/m
Membrane ionic conductivity (humidified Nafion®117)	λ_m	17.1223	S/m
Transfer coefficient, anode side	α_a	0.5	-
Transfer coefficient, cathode side	α_c	1	-
Cathode reference exchange current density	$i_{o,c}^{ref}$	1.8081e-3	A/m^2
Anode reference exchange current density	$i_{o,a}^{ref}$	2465.598	A/m^2
Electrode thermal conductivity	k_{eff}	1.3	$W/m.K$
Membrane thermal conductivity	k_{mem}	0.455	$W/m.K$
Electrode hydraulic permeability	Kp	1.76e-11	m^2
Entropy change of cathode side reaction	ΔS	-326.36	$J/mole.K$
Heat transfer coefficient between solid and gas phase	β	4e6	W/m^3
Protonic diffusion coefficient	D_{H^+}	4.5e-9	m^2/s
Fixed-charge concentration	c_f	1200	$mole/m^3$
Fixed-site charge	z_f	-1	-
Electro-osmotic drag coefficient	n_d	2.5	-

 ©2012 International Energy & Environment Foundation. All rights reserved.

Table 2. Geometrical and operational parameters for base case conditions

Parameter	***Sym.***	**Value**	**Unit**
Cell length	L	0.49×10^{-3}	m
Cell width	W	3×10^{-3}	m
Hydrogen channel diameter	D_{H2}	1×10^{-3}	m
Gas diffusion layer thickness	δ_{GDL}	0.26e-3	m
Wet membrane thickness (Nafion® 117)	δ_{mem}	0.23e-3	m
Catalyst layer thickness	δ_{CL}	0.0287e-3	m
Hydrogen reference mole fraction	$x_{H_2}^{ref}$	0.84639	-
Oxygen reference mole fraction	$x_{O_2}^{ref}$	0.17774	-
Fuel pressure	P_{fuel}	1	atm
Ambient pressure	P_{amb}	1	atm
Ambient temperature	T_{amb}	300.15	K
Fuel stoichiometric flow ratio	ξ_a	2	-

Figure 6 shows the local current density distribution at the cathode side catalyst layer for two different nominal current densities. The local current densities have been normalized by the nominal current density in each case (i.e. ic/I). It can be seen that for a low nominal current density, the distribution is quite uniform. This change for high current density, where a noticeable decrease takes place along the cell width of the electrode. It can be seen that for a high nominal current density, a high fraction of the current is generated at the catalyst layer near the air inlet area, leading to under-utilization of the catalyst at the end of the cell width of the electrode. For optimal fuel cell performance, a uniform current density generation is desirable, and this could only be achieved with a non-uniform catalyst distribution, possibly in conjunction with non-homogeneous gas diffusion layers.

The variation of the cathode activation overpotentials (in V) is shown in Figure 7. For both nominal current densities, the distribution patterns of activation overpotentials are similar, with higher values at the catalyst layer near the air inlet area. It can be seen that the activation overpotential profile correlates with the local current density, where the current densities are highest near the air inlet area and coincide with the highest reactant concentrations.

To perform a comprehensive parametric study for each components of the cell, two types of ohmic losses that occur in MEA are characterized. These are potential losses due to electron transport through electrodes and potential loss due to proton transport through the membrane. Ohmic overpotential is the loss associated with resistance to electron transport in the GDLs. For a given nominal current density, the magnitude of this overpotential is dependent on the path of the electrons. The potential field (in V) in the cathodic and the anodic gas diffusion electrodes are shown in Figure 8. The potential distributions are normal to the flow inlet of fuel and air where electrons flow into the bipolar plates. The distributions exhibit gradients in both cell width and height directions due to the non-uniform local current production and show that ohmic losses are larger in the area of the catalyst layer near the fuel and air inlet. The potential loss in the membrane is due to resistance to proton transport across the membrane from anode catalyst layer to cathode catalyst layer. The distribution pattern of the protonic overpotential is dependent on the path travelled by the protons and the activities in the catalyst layers. Figure 9 shows the potential loss distribution (in V) in the membrane for two nominal current densities. It can be seen that at a low current density, the potential drop is more uniformly distributed across the membrane. This is because of the smaller gradient of the hydrogen concentration distribution at the anode catalyst layer due to the higher diffusivity of the hydrogen.

The variation of the cathode diffusion overpotentials (in V) is shown in Figure 10. For both nominal current densities, the distribution patterns of diffusion overpotentials are similar, with higher values at the catalyst layer near the air inlet area. It can be seen that the diffusion overpotential profile correlates with the local current density, where the current densities are highest near the air inlet area and coincide with the highest reactant concentrations.

 ©2012 International Energy & Environment Foundation. All rights reserved.

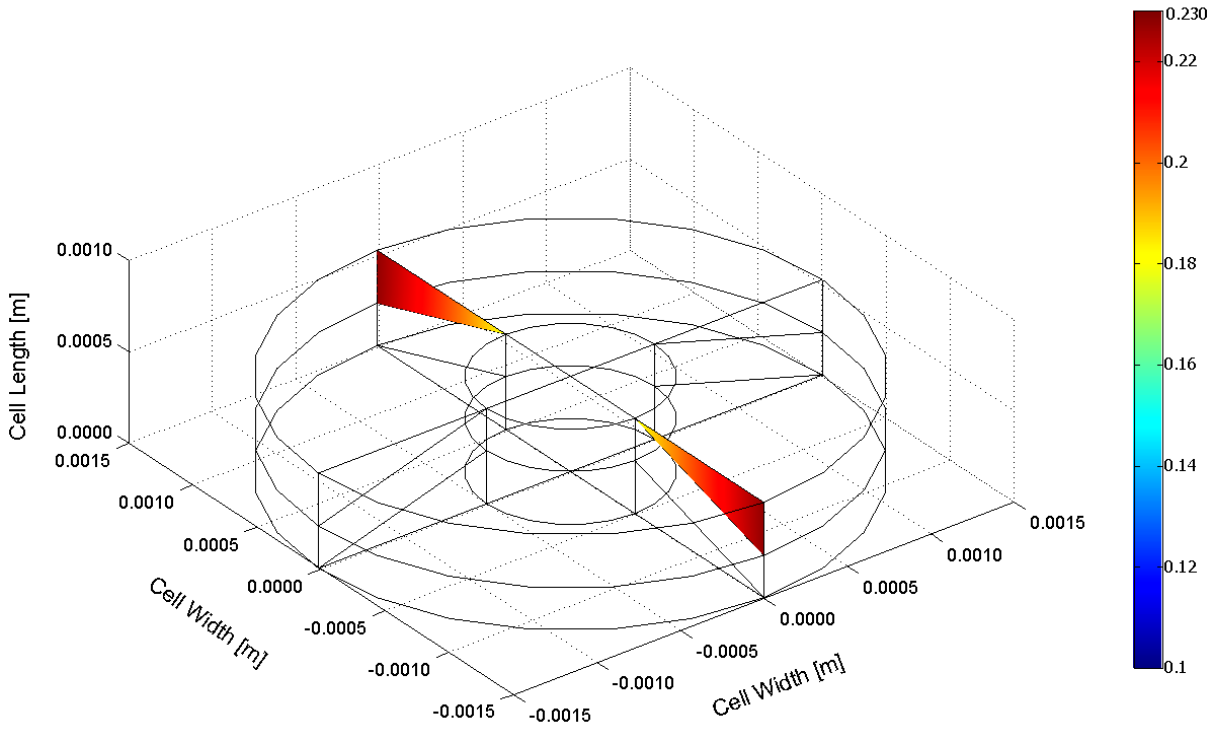

(a)

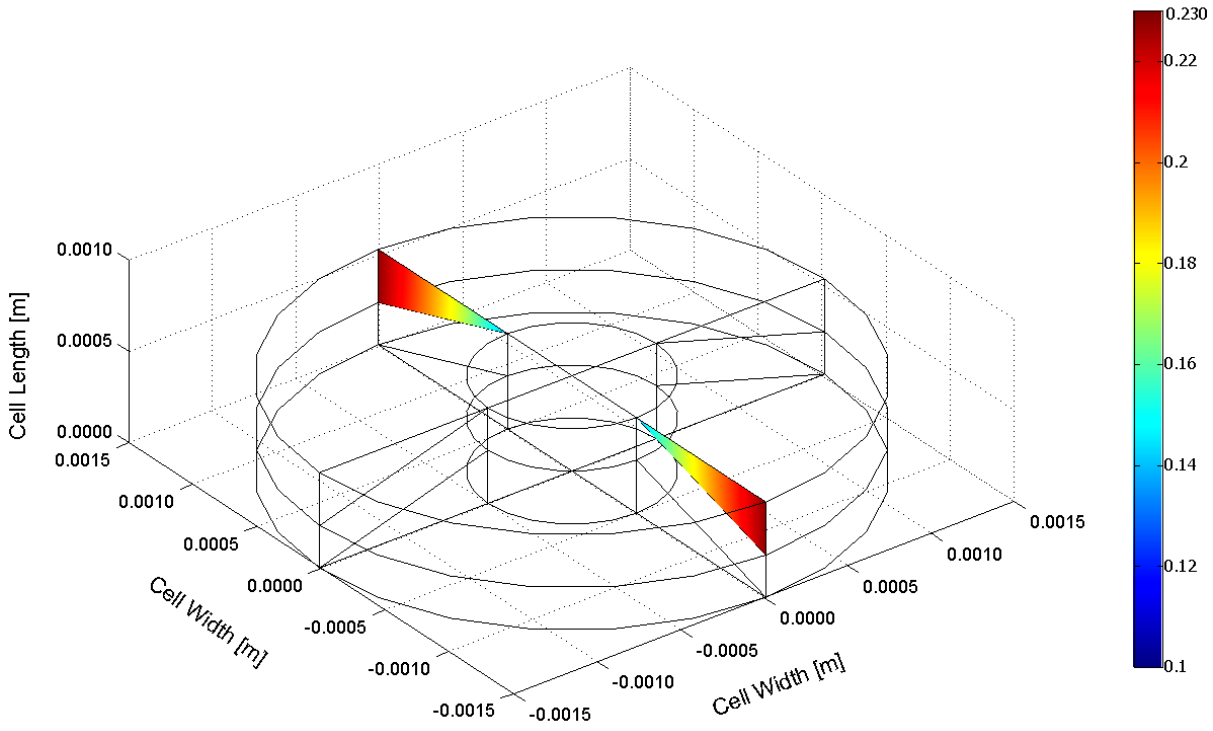

(b)

Figure 3. Oxygen mass fraction distribution in the cathode side for two different nominal current densities: (a) 0.2 A/cm^2, and (b) 0.4 A/cm^2

 ©2012 International Energy & Environment Foundation. All rights reserved.

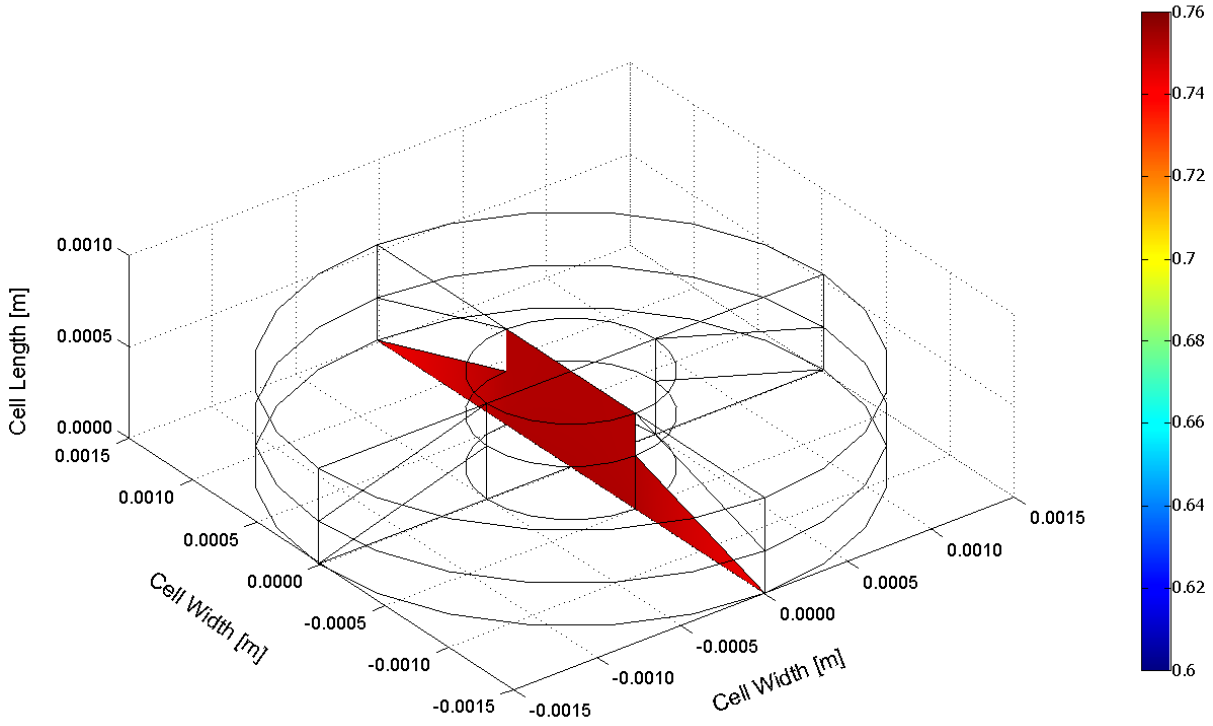

(a)

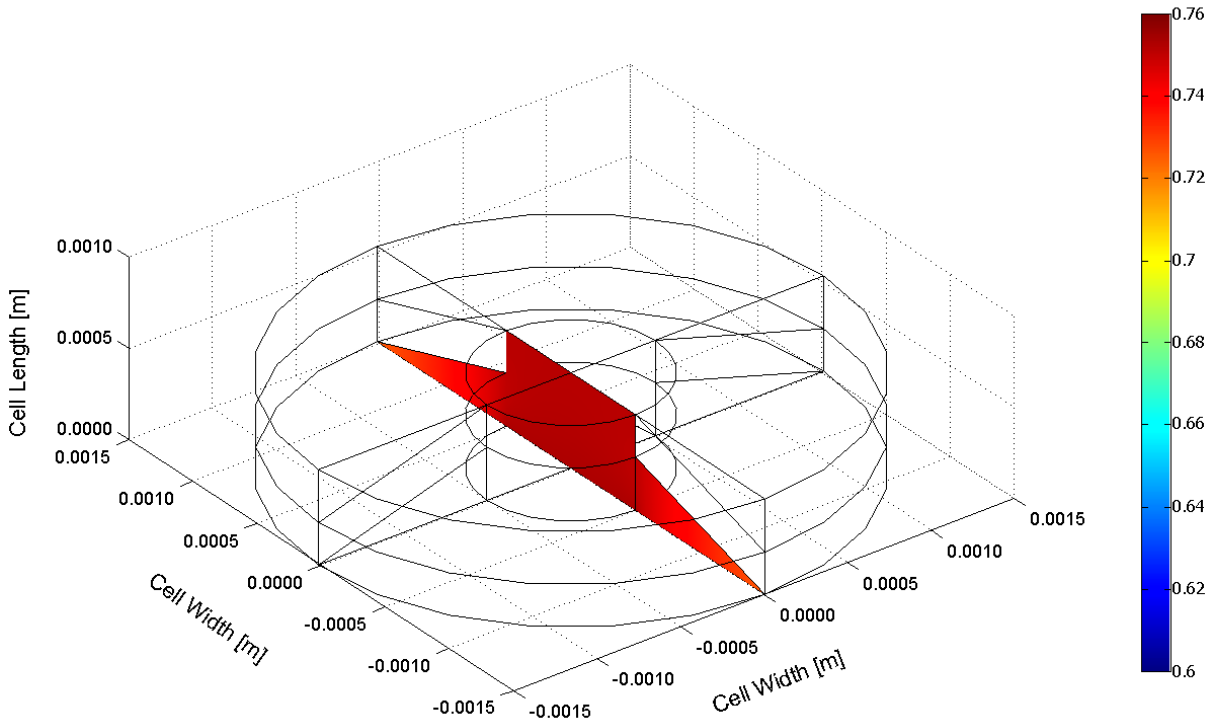

(b)

Figure 4. Hydrogen mass fraction distribution in the anode side for two different nominal current densities: (a) 0.2 A/cm^2 and (b) 0.4 A/cm^2

 ©2012 International Energy & Environment Foundation. All rights reserved.

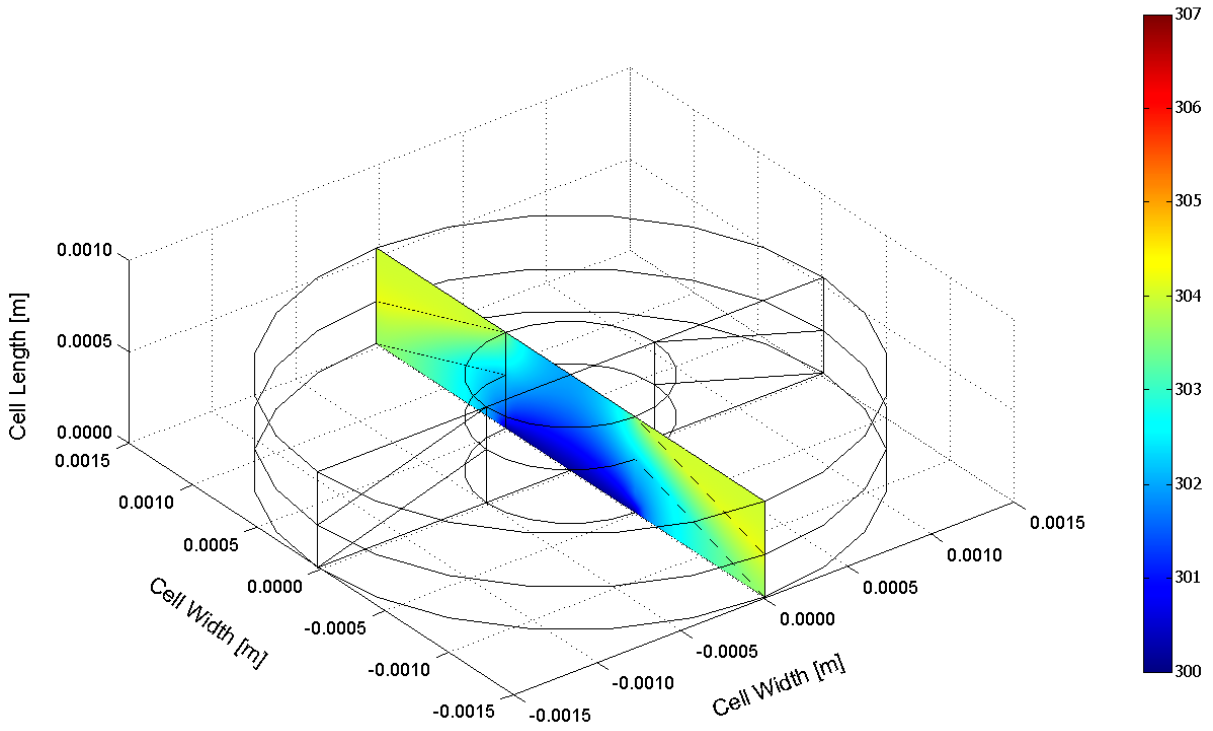

(a)

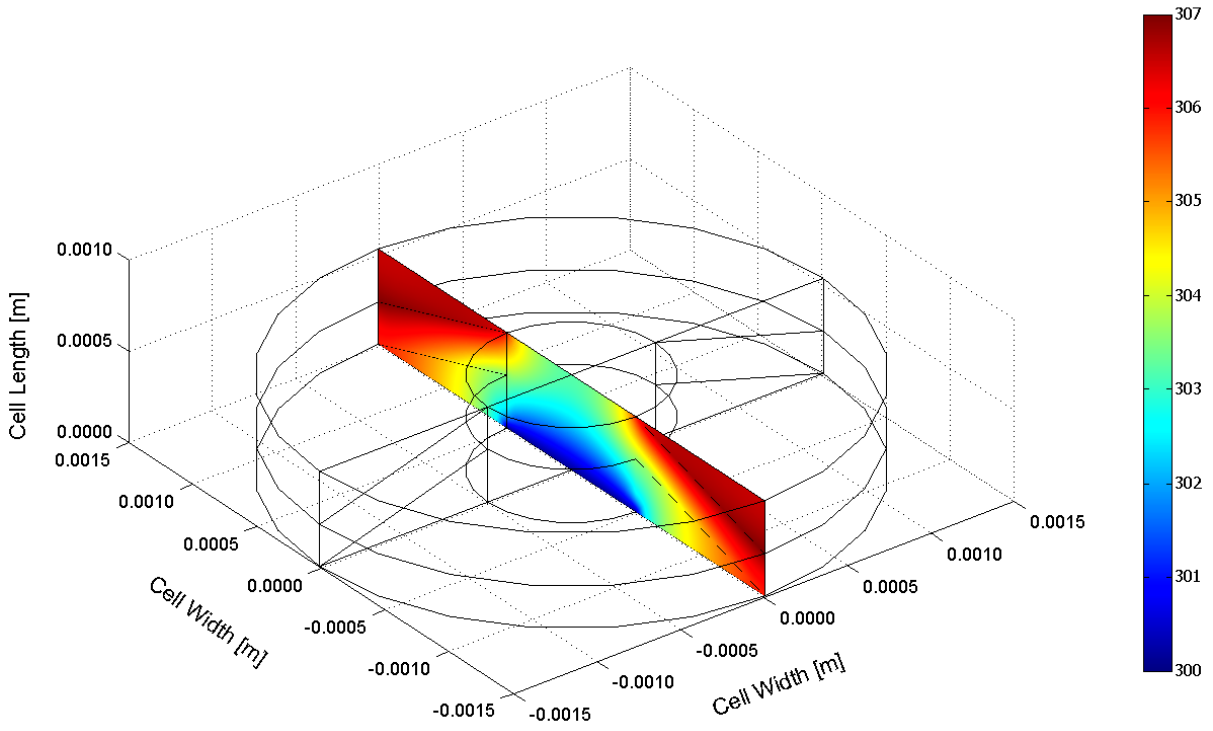

(b)

Figure 5. Temperature distribution inside the cell for two different nominal current densities: (a) 0.2 A/cm^2 and (b) 0.4 A/cm^2

 ©2012 International Energy & Environment Foundation. All rights reserved.

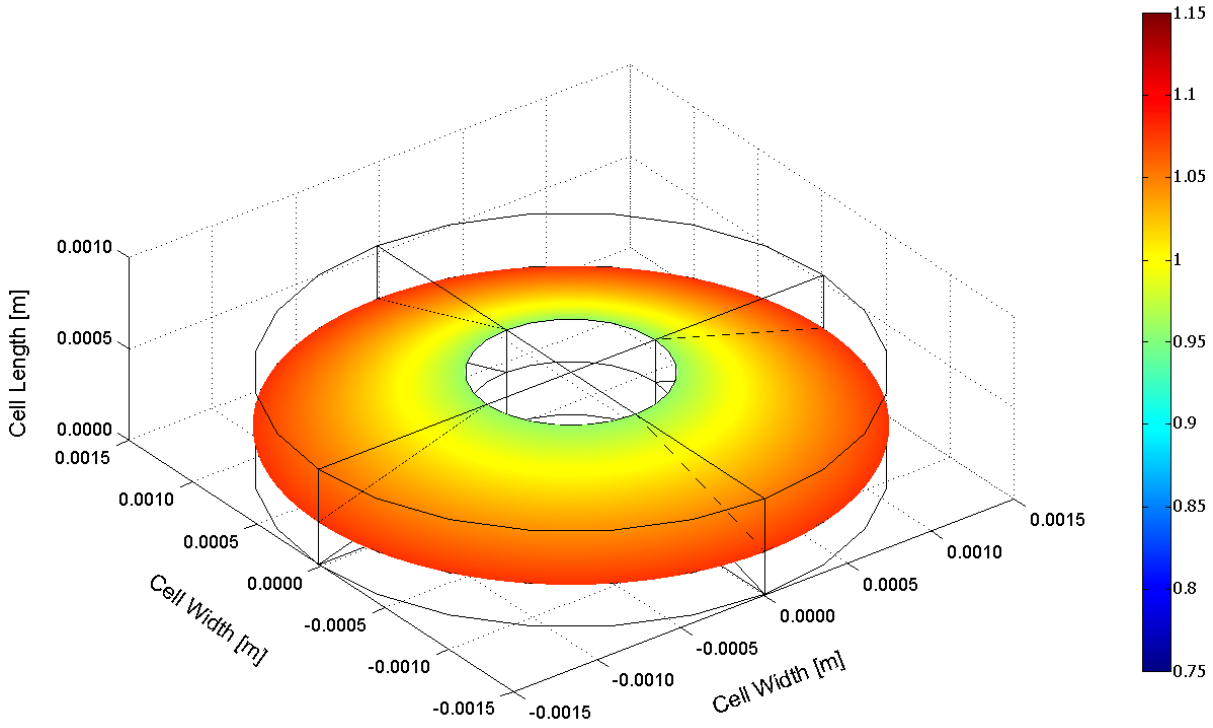

(a)

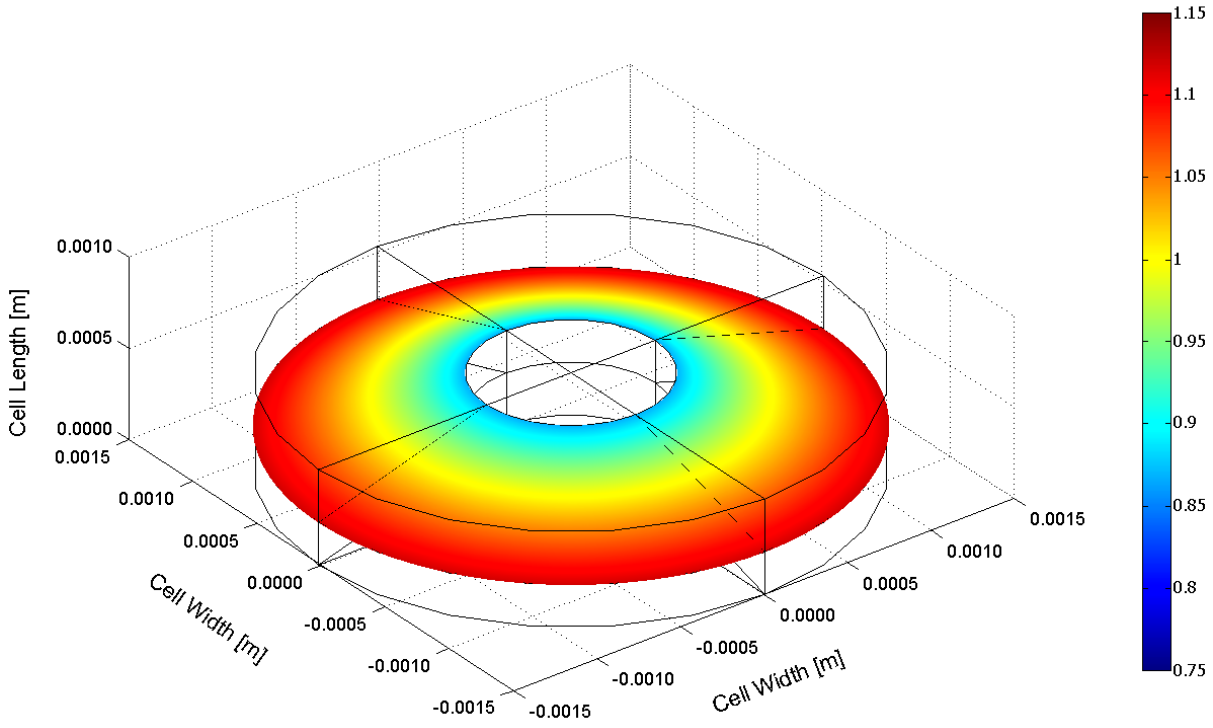

(b)

Figure 6. Local current density distribution at the cathode catalyst layer for two different nominal current densities: (a) 0.2 A/cm^2 and (b) 0.4 A/cm^2

 ©2012 International Energy & Environment Foundation. All rights reserved.

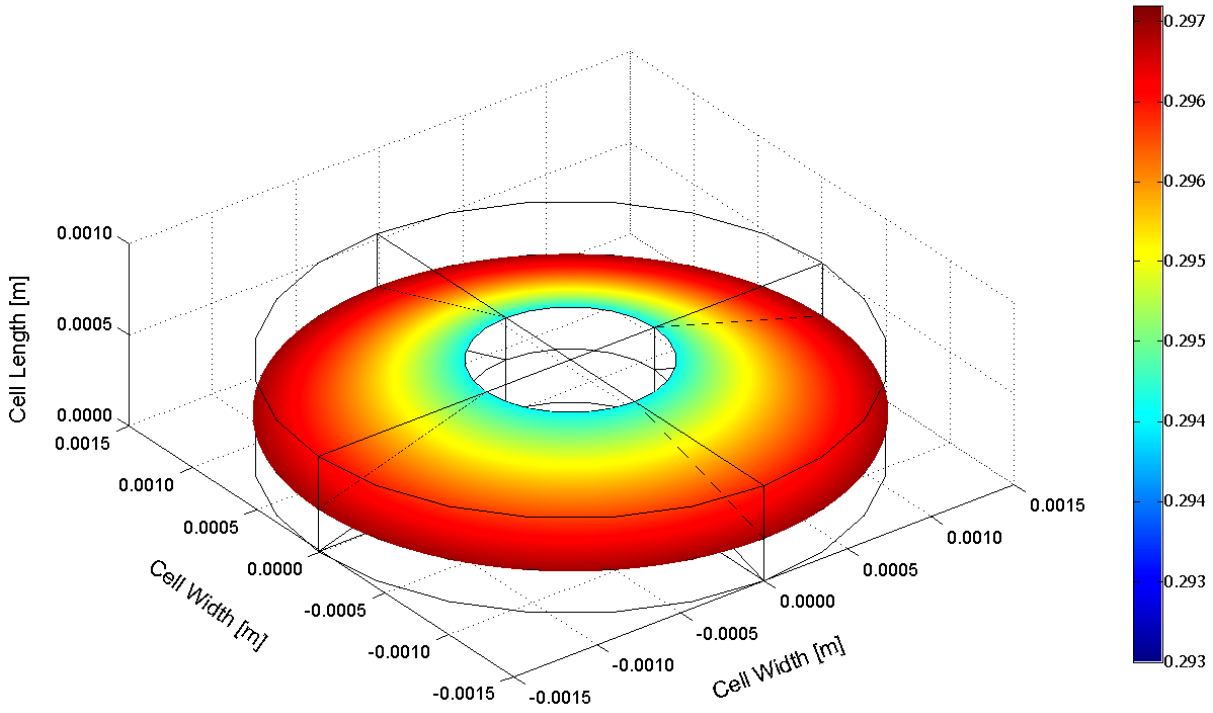

(a)

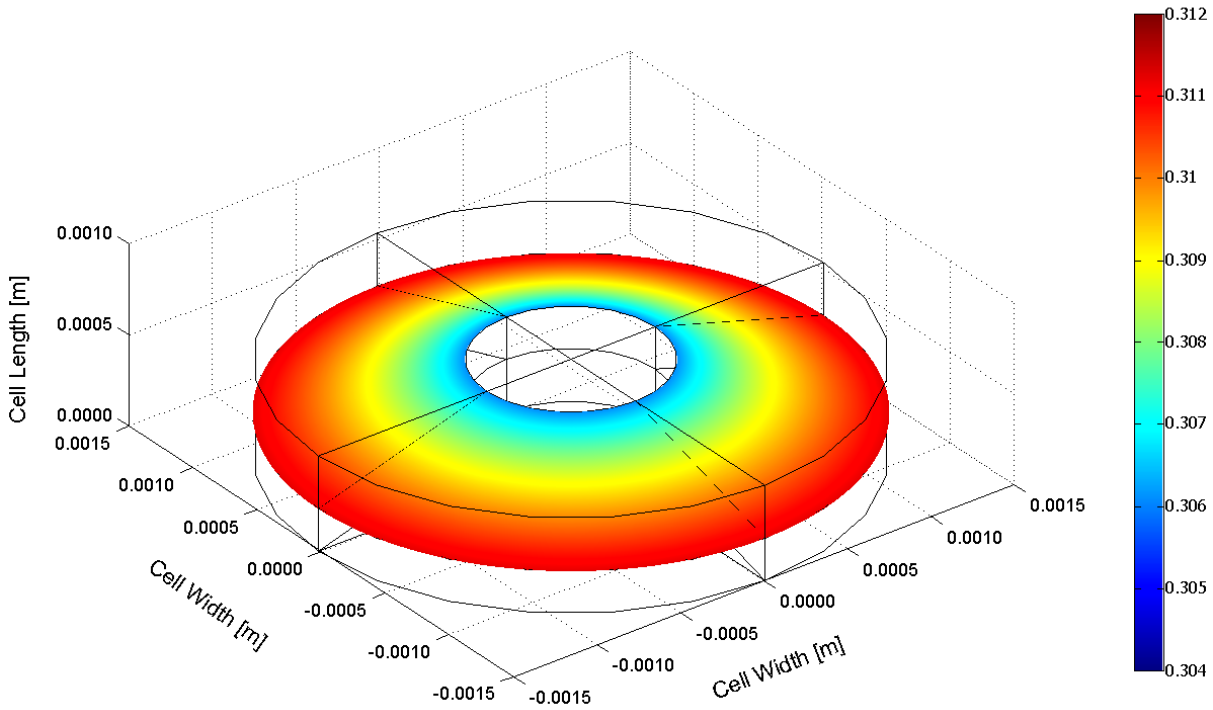

(b)

Figure 7. Activation overpotential distribution at the cathode catalyst layer for two different nominal current densities: (a) 0.2 A/cm^2 and (b) 0.4 A/cm^2

ISSN 2076-2895 (Print), ISSN 2076-2909 (Online) ©2012 International Energy & Environment Foundation. All rights reserved.

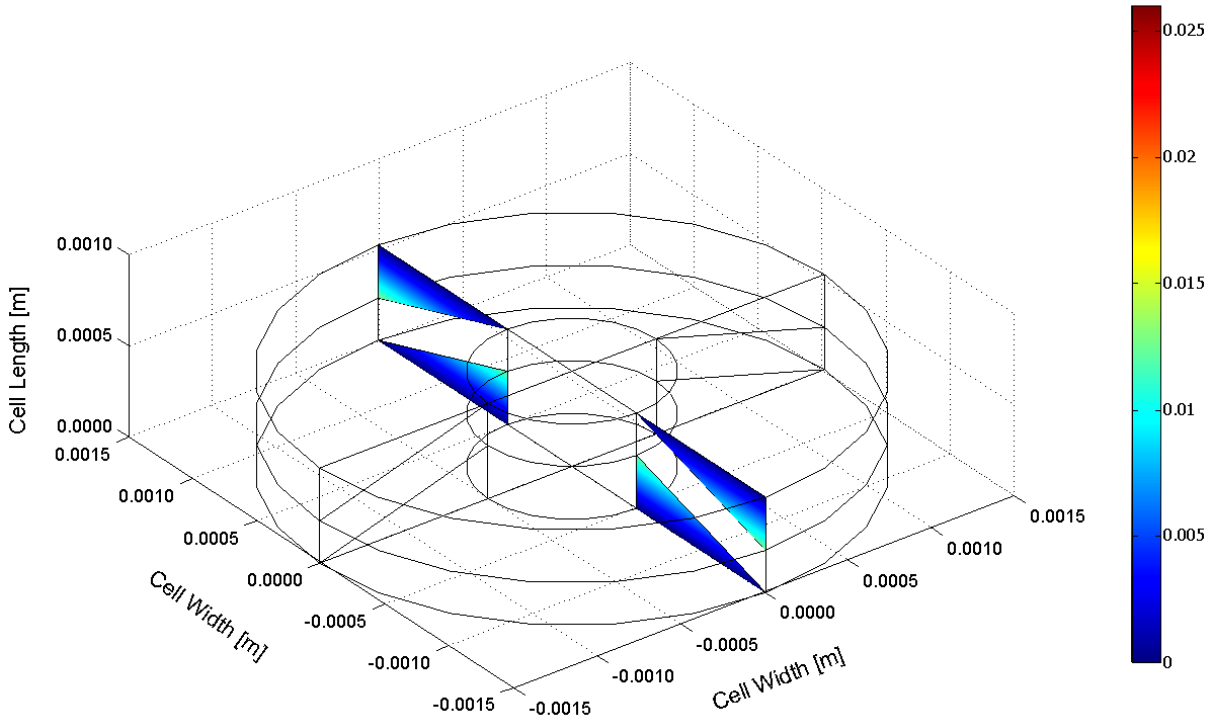

(a)

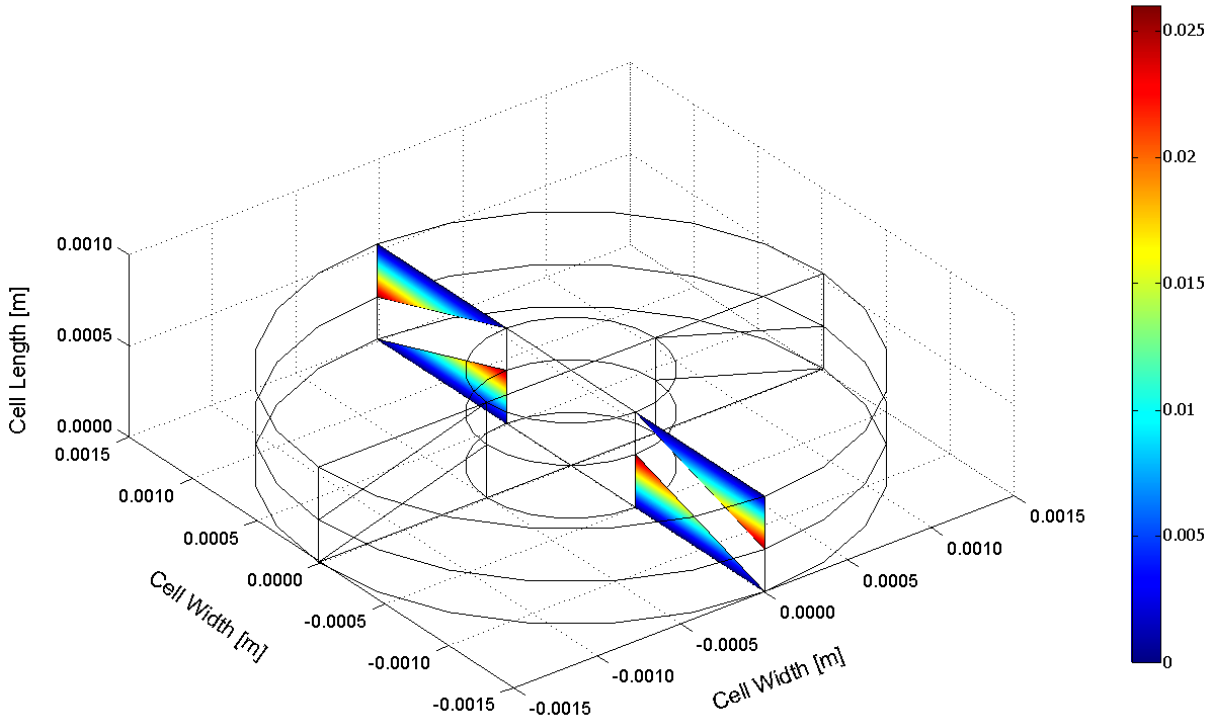

(b)

Figure 8. Ohmic overpotential distribution in the anode and cathode GDLs for two different nominal current densities: (a) 0.2 A/cm^2 and (b) 0.4 A/cm^2

 ©2012 International Energy & Environment Foundation. All rights reserved.

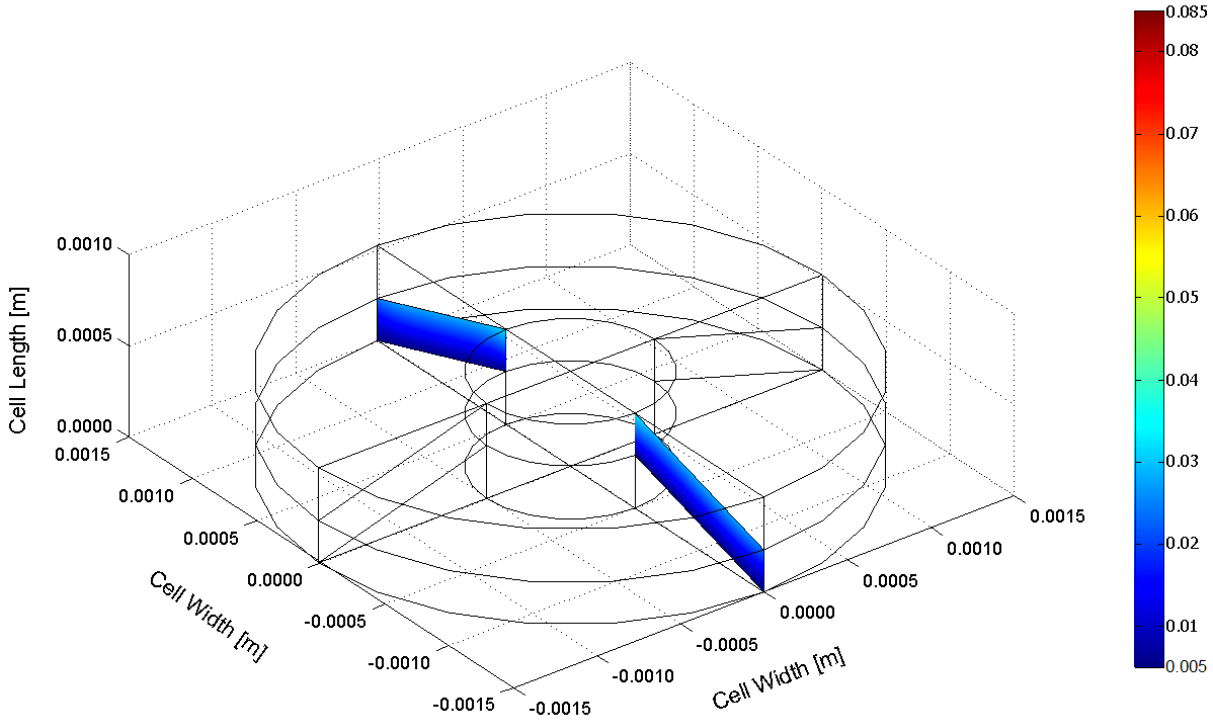

(a)

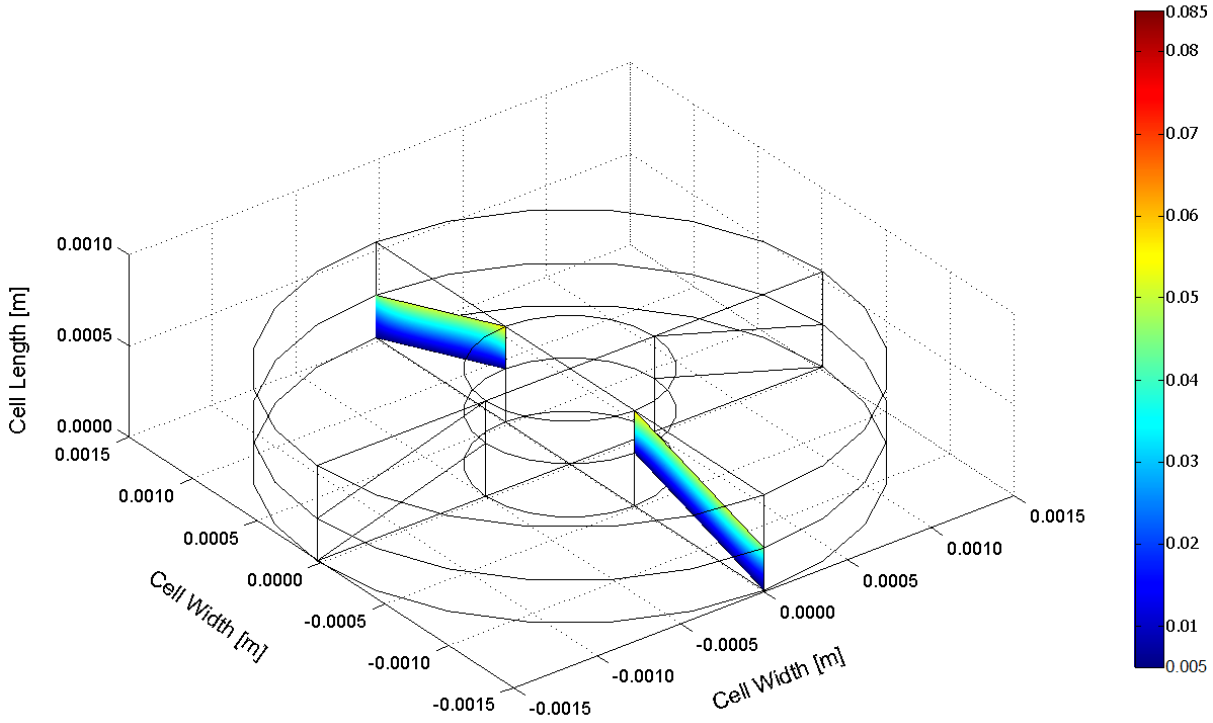

(b)

Figure 9. Membrane overpotential distribution across the membrane for two different nominal current densities: (a) 0.2 A/cm^2 and (b) 0.4 A/cm^2

 ©2012 International Energy & Environment Foundation. All rights reserved.

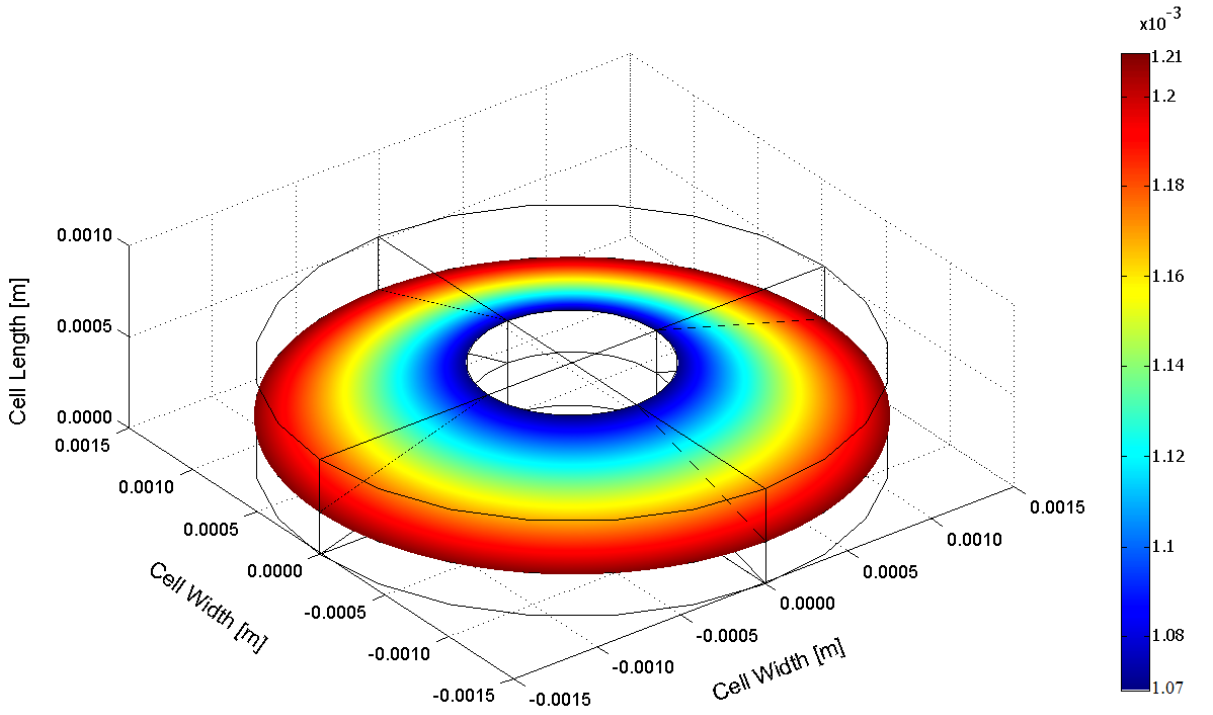

(a)

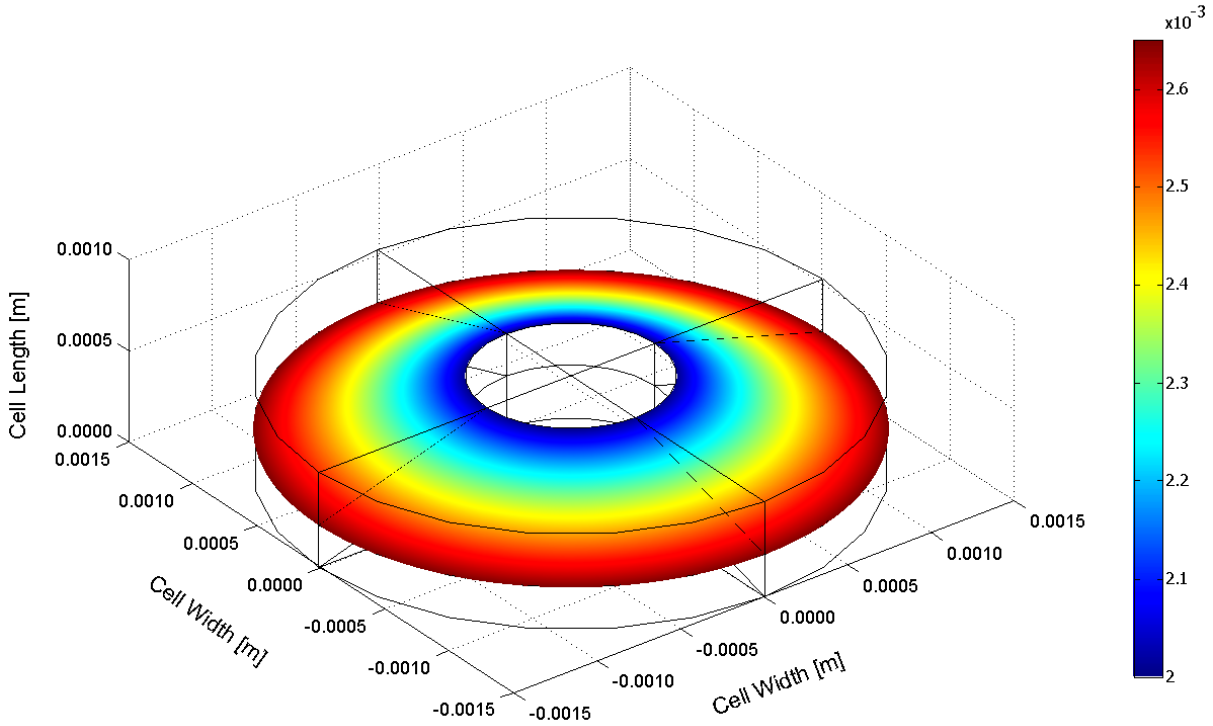

(b)

Figure 10. Diffusion overpotential distribution at the cathode catalyst layer for two different nominal current densities: (a) 0.2 A/cm^2 and (b) 0.4 A/cm^2

 ©2012 International Energy & Environment Foundation. All rights reserved.

4. Conclusions

A full three-dimensional CFD model of a novel design disk-shaped air-breathing micro-structured PEM fuel cell has been developed. The results show that higher volumetric power densities are achieved with this design mainly because of higher active area to volume ratios. The model is shown to be able to:

(1) understand the many interacting, complex electrochemical and transport phenomena that cannot be studied experimentally;
(2) identify limiting steps and components; and
(3) provide a computer-aided tool for the design and optimization of future fuel cells to improve their lifetime with a much higher power density and lower cost.

The analysis offers valuable physical insight towards design of a cell and a cell stack, to be considered in a future study.

References

[1] Litster S. and Djilali N. Mathematical modelling of ambient air-breathing fuel cells for portable devices. Electrochimica Acta J. 2007, 52(11), 3849-3862.
[2] O'Hayre R., Fabian T., Litster S., Prinz F.B., Santiago J.G. Engineering model of a passive planar air breathing fuel cell cathode. J. Power Sources. 2007, 167(1), 118–129.
[3] Rajani B.P.M. and Kolar A.K. A model for a vertical planar air breathing PEM fuel cell. J. Power Sources 2007, 164(1), 210-221.
[4] Hwang J.J., Wu S.D., Pen R.G., Chen P.Y., and Chao C.H. Mass/electron co-transports in an air-breathing cathode of a PEM fuel cell. J. Power Sources 2006, 160(1), 18-26.
[5] Maher A.R. Sadiq Al-Baghdadi. Performance comparison between airflow-channel and ambient air-breathing PEM fuel cells using three-dimensional computational fluid dynamics models. Renewable Energy 2009, 34(7), 1812–1824.
[6] Fuller E.N., Schettler P.D., and Giddings J.C. A new methode for prediction of binary gas-phase diffusion coefficients. Ind. Eng. Chem., 1966, 58(5), 18-27.
[7] Berning T., and Djilali N. A 3D, Multi-Phase, Multicomponent Model of the Cathode and Anode of a PEM Fuel Cell. J. Electrochem. Soc., 2003, 150(12), A1589-A1598.
[8] Nguyen P.T., Berning T., and Djilali N. Computational Model of a PEM Fuel Cell with Serpentine Gas Flow Channels. J. Power Sources, 2004, 130(1-2), 149-157.
[9] Berning T., Lu D.M., and Djilali N. Three-Dimensional Computational Analysis of Transport Phenomena in a PEM Fuel Cell. J. Power Sources, 2002, 106(1-2), 284-294.
[10] Maher A.R. Sadiq Al-Baghdadi. A CFD study of hygro-thermal stresses distribution in tubular-shaped ambient air-breathing PEM micro fuel cell during regular cell operation. International Journal of Energy and Environment, 2010, 1(2), 183-198.
[11] Lampinen M.J., and Fomino M. Analysis of free energy and entropy changes for half-cell reactions, J. Electrochem. Soc., 1993; 140(12), 3537–3546.
[12] Siegel N.P., Ellis M.W., Nelson D.J., and Spakovsky M.R. von. A two-dimensional computational model of a PEMFC with liquid water transport. J. Power Sources, 2004, 128(2), 173–184.
[13] Hu M., Gu A., Wang M., Zhu X., and Yu L., Three dimensional, two phase flow mathematical model for PEM fuel cell. Part I. Model development, Energy Conversion Manage, 2004; 45(11-12): 1861–1882.
[14] Maher A.R. Sadiq Al-Baghdadi. Modeling optimizes PEM fuel cell durability using three-dimensional multi-phase computational fluid dynamics model. International Journal of Energy and Environment IJEE, 2010; 1(3), 375-398.
[15] Maher A.R. Sadiq Al-Baghdadi. Mechanical behaviour of PEM fuel cell catalyst layers during regular cell operation. International Journal of Energy and Environment, 2010; 1(6), 927-936.
[16] Maher A.R. Sadiq Al-Baghdadi. A CFD analysis on the effect of ambient conditions on the hygro-thermal stresses distribution in a planar ambient air-breathing PEM fuel cell. International Journal of Energy and Environment, 2011; 2(4), 589-604.
[17] F. Brèque, J. Ramousse, Y. Dubé, K. Agbossou, P. Adzakpa. Sensibility study of flooding and drying issues to the operating conditions in PEM Fuel Cells. International Journal of Energy and Environment IJEE, 2010; 1(1), 1-20.

 ©2012 International Energy & Environment Foundation. All rights reserved.

[18] Maher A.R. Sadiq Al-Baghdadi. Optimal design of PEM fuel cells to generate maximum power: A CFD study. International Journal of Energy and Environment, 2011; 2(6), 953-962.
[19] Maher A.R. Sadiq Al-Baghdadi. Novel design of a compacted micro-structured air-breathing PEM fuel cell as a power source for mobile phones. International Journal of Energy and Environment IJEE, 2010; 1(4), 555-572.

ISSN 2076-2895 (Print), ISSN 2076-2909 (Online) ©2012 International Energy & Environment Foundation. All rights reserved.